RSC Advances

PAPER

View Article Online
View Journal | View Issue

Cite this: *RSC Adv.*, 2025, **15**, 22875

Anticancer efficacy of bis-heteroleptic iridium(III) complexes with difluoro-substituted phenylpyridine ligands†

Suvasmita Behera,[ab] Kahnu Charan Pradhan,[ab] Sahadev Barik,[c] Moloy Sarkar,[c] Jagadish Kumar,[d] Jagneshwar Dandapat,[e] Jyotsnarani Pradhan*[e] and Satyanarayan Pal*[ab]

Received 1st May 2025
Accepted 12th June 2025

DOI: 10.1039/d5ra03076e

rsc.li/rsc-advances

A series of iridium(III) complexes (**Ir1–Ir3**) with the formula $[Ir(F_2ppy)_2(L)]$ (F_2ppy = 2-(2,4-difluoro-phenyl) pyridine, L = pyridine-2-aldoxime, 2-pyridylamidoxime and di-2-pyridylketoxime) were synthesized through the reaction of $[(F_2ppy)_2Ir(\mu\text{-}Cl)_2Ir(F_2ppy)_2]$ (SM1) and the respective ancillary ligands (L). All the complexes were characterised by FT-IR, ^1H & ^{19}F-NMR analysis, electronic absorption–emission spectroscopy and cyclic voltammetric studies. Molecular structures of complexes **Ir1** and **Ir3** were determined by interpreting single crystal X-ray data. All the complexes were found to be luminescent with low quantum yields. Anticancer studies on cancer cell lines MDAMB, HT-29 and LN-229 revealed their effectiveness as antiproliferative agents. The cytotoxicity of the complexes was evaluated using the MTT assay and complex **Ir2** showed activity similar to that of cisplatin towards the three cancer cells. The elevated level of reactive oxygen species (ROS) in the iridium complex-treated cancer cells further supported the antiproliferation efficacy of **Ir1–Ir3**. Further, the effectiveness of **Ir1–Ir3** on cancer cells was established through a cell migration study and apoptotic induction assay on LN-229 and a colony formation assay on HT-29 cancer cells. Immunocytochemistry analysis of LN-229 cancer cells revealed apoptosis through the p53-dependent pathway.

Introduction

Iridium(III) organometallic complexes with a 2-phenylpyridine (ppy) genre backbone are found to be intrinsically luminescent.[1–4] Various substitutions on the phenyl and pyridine rings of ppy have been chosen as ligands in the design of a vast family of emissive Ir(III) complexes. The ppy ligation in Ir(III) complexes brings the HOMO–LUMO levels to the desired separation for visible light emission. An array of ppy ligands with various substitutions on phenyl rings were synthesised and complexed with an Ir(III) center for the emission of light across the visible spectrum. Among many options, the difluoro-substituted phenylpyridine, *i.e.*, 2-(2,4-difluoro-phenyl) pyridine (**HF_2ppy**) (Fig. 1), has emerged as a highly useful ligand in the design of Ir(III) luminescent materials.[5–7] A design principle of two units of phenylpyridines and a bidentate ancillary ligand (L) around the Ir(III) centre, *i.e.*, $[Ir(ppy)_2L]$, was chosen for an easy synthetic route for the target materials. Keeping the phenylpyridine backbone intact, a range of bidentate ancillary ligands have been employed to achieve Ir(III) complexes targeted for applications in various fields, such as organic light-emitting diodes (OLEDs), photo redox catalysts,[8] biological cell imaging,[9] and anticancer active agents.[10,11]

In recent developments, the composition $[Ir(ppy)_2(L)]^{+/0}$ (L = bidentate ligand) has proven to be effective in the development of anticancer active agents.[12–14] To date, results obtained from

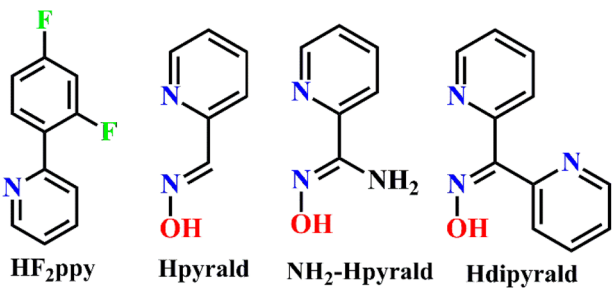

Fig. 1 List of ligands utilised.

[a]P.G. Dept. of Chemistry, Utkal University, Bhubaneswar, Odisha 751004, India. E-mail: snpal@utkaluniversity.ac.in
[b]Centre of Excellence in Advanced Materials and Applications, Utkal University, Bhubaneswar, Odisha 751004, India
[c]School of Chemical Sciences, National Institute of Science Education and Research, Bhubaneswar, Odisha 752050, India
[d]Dept. of Physics, Utkal University, Bhubaneswar, Odisha 751004, India
[e]Dept. of Biotechnology, Utkal University, Bhubaneswar, Odisha 751004, India

† Electronic supplementary information (ESI) available. CCDC 2377820 and 2377821. For ESI and crystallographic data in CIF or other electronic format see DOI: https://doi.org/10.1039/d5ra03076e

different cancer cell lines with Ir(III) complexes have displayed encouraging outcomes. Anti-cancer studies have revealed that $[Ir(ppy)_2L]^{+/0}$ type complexes can interact with DNA, mitochondria, nucleus and other organelles of the cells for cell death activities.[15,16] Complexes with the above design, $[Ir(ppy)_2(L)]^{+/0}$, have proved their potential as therapeutic agents for different cancer cells.[17–20] It is found that the coordinated ancillary ligand 'L' plays an important role in identifying and targeting the cellular parts to interact with them directly.[21–23] Thus, selecting appropriate bidentate ancillary ligands is essential for the design and development of cyclometallated iridium(III)-based anti-cancer drugs. This choice facilitates targeted drug delivery, minimizes unintended side effects, improves effectiveness with lower dosages and ultimately reduces the multidrug resistance observed in current cancer treatments.[24] In this context, we have focused on pyridine-oxime-based ancillary ligands owing to their novel therapeutic potential[25,26] and the remarkable anti-cancer activities displayed by pyridine-oxime containing metal complexes against various cancer cell lines.[27–29] Additionally, our observation of unusual coordination by 2-pyridinealdoxime (**Hpyrald**) as an ancillary ligand[30,31] in a cyclometallated Ir(III) complex further spurred the exploration of Ir(III) chemistry with an oxime-containing organic entity. Similarly, in our quest for unique properties, we recently reported three new cyclometallated Pt(II) complexes featuring 2-pyridinealdoxime (**Hpyrald**) and investigated their cancer therapeutic potential against MCF-7 and MDAMB-231 cells.[32] The findings revealed that the [Pt(F_2ppy)(pyrald)] complex is a proficient anticancer agent. However, the complex demonstrated lower anticancer activity than cisplatin. In contrast, our previously reported Ir(III) complexes with fluorine-substituted cyclometallating ligands[33] and other F_2ppy-containing Ir(III) complexes in the literature showed greater anticancer efficacy than cisplatin.[34] Therefore, we believe that the anticancer potential can be effectively tuned by altering the central metal atom to Ir(III) and employing different structural arrangements of the F_2ppy and pyrald ligands (Fig. 1). We designed a series of complexes with the general formula **[Ir(F_2ppy)$_2$(L)]** (where L = pyridine-2-aldoxime and substituted pyridine-2-aldoxime) (Fig. 2). The substitution of **Hpyrald** with $-NH_2$ and a free pendant pyridine moiety was selected considering the effective anticancer activity demonstrated by cyclometallated iridium(III) complexes containing free amine and aromatic rings.[24,34,35]

Hence, extending our study on oxime-containing Ir(III) chemistry, herein, we report three iridium complexes and explore their luminescent behaviour, structural properties and therapeutic potentials.

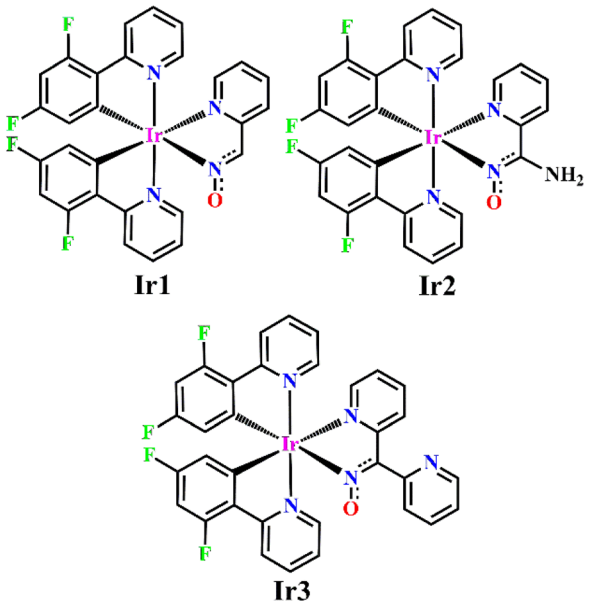

Fig. 2 Structure of prepared iridium(III) complexes.

Results and discussion

Synthesis and some properties

All the complexes were synthesised in moderate to high yields under mild conditions and are found to be highly air and moisture stable. In **Ir1**, deprotonated pyridine-2-aldoxime (**pyrald**) coordinated the iridium(III) metal centre through pyridine-*N* and aldoxime-*N* atoms and identical binding modes of ancillary ligands were observed in complexes **Ir2** and **Ir3** although ligands 2-pyridylamidoxime (**NH_2pyrald**) and 2-dipyridylketoxime (**dipyrald**) have other possible coordination modes (Fig. 2). **NH_2pyrald** can coordinate through the pyridine-*N* and $-NH_2$ group, while the **dipyrald** can coordinate through two pyridine-*N* atoms.[36] The ligations of ancillary ligands to the metal center were confirmed from the single crystal X-ray analysis and NMR spectra of the complexes. The appearance of a broad peak at 5.81 ppm in the proton NMR spectrum indicated the existence of the free $-NH_2$ group in **Ir2** and supported the coordination of pyridine-*N* and aldoxime-*N* for **NH_2pyrald**. The base peaks observed in the mass spectra of complexes were found to be well-matched with the theoretical mass of the complexes. Furthermore, the observed four fluorine signals in the ^{19}F NMR spectra of **Ir1–Ir3** in the range of 107–111 ppm indicated the coordination of two F_2ppy ligands. All the complexes were found to be soluble in methanol, ethanol, acetonitrile and acetone solvents. The complex [Ir(F_2ppy)$_2$(NH_2pyrald)] (**Ir2**) was also found to be partly soluble in water owing to the presence of the free $-NH_2$ group.

Structural characterisation

The single crystal X-ray structures of [Ir(F_2ppy)$_2$(pyrald)] + CH_3OH (**Ir1·CH_3OH**) and [Ir(F_2ppy)$_2$(dipyrald)] (**Ir3**) are depicted in Fig. 3a and b, respectively. The crystal structure of **Ir1** revealed to contain methanol as the solvent of crystallisation, and the core **Ir1** and **Ir3** molecular structures depicted the coordination of two F_2ppy and one molecule of **pyrald** or **dipyrald** around each Ir(III) centre in a distorted octahedral geometry. This is in agreement with the bidentate nature of the coordinating ligands.

In the coordination sphere, the F_2ppy ligands tethered the iridium centre through "N" and "C" and the two "N"s (N1 and N2) were found in trans positions in the coordination sphere. The carbon atoms (C11 and C22) of F_2ppy ligands were in cis

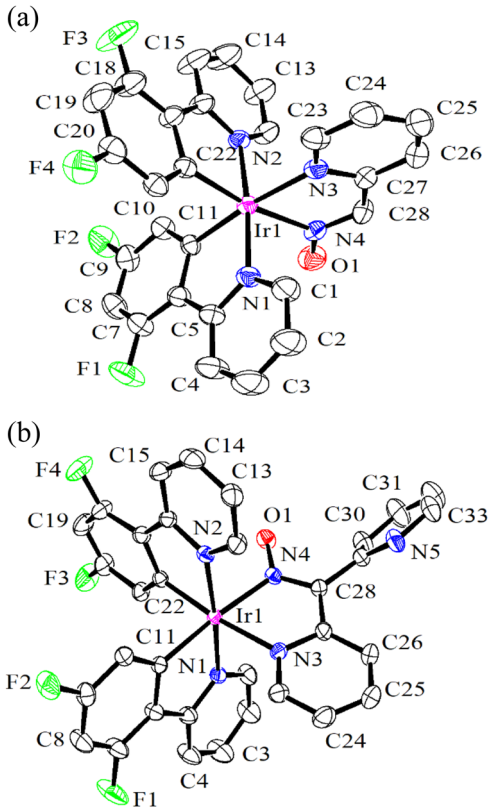

Fig. 3 (a) Thermal ellipsoid plot (40%) of [Ir(F_2ppy) (pyrald)] + CH_3OH (**Ir1·CH_3OH**). Hydrogen atoms and methanol were excluded for clarity. (b) Thermal ellipsoid plot (30%) of [Ir(F_2ppy) (dipyrald)] (**Ir3**). Hydrogen atoms were excluded for clarity.

positions and made a square plane along with N3 and N4 of the **pyrald/dipyrald** ligand. The Ir–C bond distances [2.005(5) and 2.021(4)] of **Ir1** were in good agreement with the reported structure of iridium(III) complexes containing F_2ppy ligands.[7] The bond distances of Ir–N1 and Ir–N2 [2.046(3) Å and 2.051(3) Å] of F_2ppy origin in **Ir1** were found to be shorter than the Ir–N3 and Ir–N4 bond distances [2.116(3) Å and 2.119(5) Å] emanated from pyrald ligand, respectively. This Ir–N bond distance disparity was due to the strong trans influence exerted by coordinating C11 and C22 situated at the trans position to N3 and N4, respectively, in the coordination sphere. A very similar coordination sphere was found in **Ir3** with bond lengths and angles comparable to **Ir1·CH_3OH** (Table 1).

Theoretical studies

The DFT and TD-DFT methods were used to study the quantum mechanical calculation of all three iridium complexes **Ir1–Ir3**. The $S_0 \rightarrow S_1$ transitions along with corresponding HOMO → LUMO transitions are shown in Fig. S16† and Table 2. The HOMO–LUMO electronic population with the corresponding energy gaps of **Ir1–Ir3** is depicted in Fig. 4.

The HOMOs of **Ir1–Ir3** mainly spread over ancillary ligands with a minimal distribution on iridium(III) centres. In contrast, the LUMOs had a dominant contribution of cyclometallating F_2ppy ligands (Fig. 4 and S16†). Despite the structural difference of ancillary ligands, the highest occupied frontier molecular orbitals (HOMO) of **Ir1** and **Ir3** were found to have approximately the same energy values, *i.e.* ~5.19 eV. Similar observations were made for the LUMO energy levels of **Ir1** and **Ir3**, with the lowest energy levels at −1.52 eV and −1.53 eV, respectively. This could be due to the non-involvement of the pyridine substituent in the formation of HOMO and LUMO in **Ir3** (Fig. S16†).

The HOMO–LUMO energy gap in **Ir2** was found to be the lowest, *i.e.* 3.08 eV, and it was ascribed to the high-lying HOMO (−4.59 eV) of **Ir2** among the three complexes. As the LUMOs of all three complexes had comparable energies (1.50–1.53 eV), the high lying HOMO caused the smallest separation of HOMO–LUMO in **Ir2**.

Optoelectronic studies

The UV-visible spectra of the three iridium complexes were taken in acetonitrile solution at room temperature within a concentration range of 10^{-5} mol per L. Complexes **Ir1–Ir3** exhibited intense absorption spectra at 255, 251 and 254 nm, respectively (Fig. 5). These high energy transitions were assigned to the ligand-centered $\pi \rightarrow \pi^*$ transitions. The next few weak bands were obtained at 371, 365 and 375 nm for complex **Ir1–Ir3**, respectively (Fig. 5). These transitions could be attributed to the combination of spin-allowed charge transfer spectra. Further, the appearance of the least intense peaks in the visible region might have originated from the spin-forbidden electronic transitions involving ^{3}MLCT, ^{3}LLCT or ^{3}ILCT.

From the TD-DFT calculation, the percentage contributions of iridium, cyclometallating ligands and ancillary ligands in HOMOs and corresponding LUMOs are presented in Table S1.† HOMOs mainly spread over ancillary ligands with minimal

Table 1 Selected bond lengths and angles of [Ir(F_2ppy)$_2$(pyrald)] + CH_3OH (**Ir1·CH_3OH**) and [Ir(F_2ppy)$_2$(dipyrald)] (**Ir3**)

Ir1				**Ir3**			
Bond lengths [Å]		Bond angles [°]		Bond lengths [Å]		Bond angles [°]	
Ir1–C11	2.005 (5)	N1–Ir1–N2	174.83 (13)	Ir1–C11	2.030 (3)	N1–Ir1–N2	175.63 (11)
Ir1–C22	2.021 (4)	C11–Ir1–N3	173.71 (15)	Ir1–C22	2.014 (3)	C11–Ir1–N3	99.41 (12)
Ir1–N1	2.046 (3)	C11–Ir1–C22	88.92 (16)	Ir1–N1	2.041 (3)	C11–Ir1–C22	85.64 (13)
Ir1–N2	2.051 (3)	C22–Ir1–N3	95.86 (15)	Ir1–N2	2.041 (3)	C22–Ir1–N3	174.02 (11)
Ir1–N3	2.116 (3)	N3–Ir1–N4	77.18 (13)	Ir1–N3	2.122 (3)	N3–Ir1–N4	76.89 (11)
Ir1–N4	2.119 (5)	C11–Ir1–N4	98.52 (15)	Ir1–N4	2.086 (3)	C11–Ir1–N4	174.73 (12)

Table 2 Theoretically calculated electronic transitions and contours of HOMOs and LUMOs in complex **Ir1–Ir3** [a]

Complex	Nature of transitions $S_0 \rightarrow S_1$	Wavelength (nm)	Oscillator strength (f)	Contour of orbitals	
				HOMO	LUMO
Ir1	HOMO → LUMO π/d → π* L′LCT/MLCT/L′MCT	389.7	0.0114	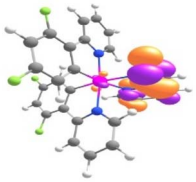 π_{pyrald}/d_{Ir}	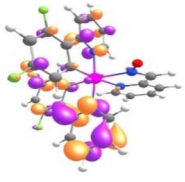 $\pi^*_{(F2ppy)}/d_{Ir}$
Ir2	HOMO → LUMO π/d → π* L′LCT/MLCT/L′MCT	380.9	0.0131	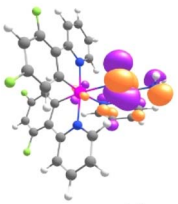 $\pi_{NH2pyrald}/d_{Ir}$	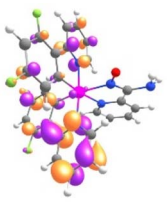 $\pi^*_{(F2ppy)}/d_{Ir}$
Ir3	HOMO → LUMO π/d → π* L′LCT/MLCT/L′MCT	386.2	0.0158	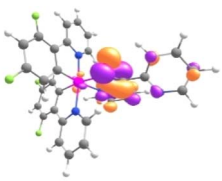 $\pi_{dipyrald}/d_{Ir}$	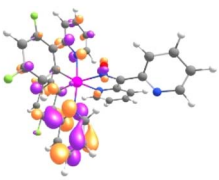 $\pi^*_{(F2ppy)}/d_{Ir}$

[a] L = F_2ppy, L′ = ancillary ligands (**pyrald**, **NH_2pyrald** and **dipyrald** for **Ir1–Ir3**, respectively).

contribution of the iridium atom, and the corresponding LUMOs were dominantly found on cyclometallating ligands with negligible contribution of iridium d-orbitals (Fig. S16 and Table S1†).

To reveal the origin of the absorption bands, the results of TD-DFT calculations of all three iridium complexes were analysed. The experimental and theoretically calculated peaks with the highest oscillatory strengths were compared, as illustrated in Table S2 in the ESI.† It revealed that the absorption bands in the region 365–375 nm mainly originated from HOMO–LUMO transitions with a minimum share of HOMO−1 to LUMO+1 transitions. The characteristics of these transitions were found to be a mixture of singlet L′LCT, MLCT and L′MCT origin (L′ = ancillary ligand). The ^{1}L′LCT character was found to be superior over all other possible transitions in the present three

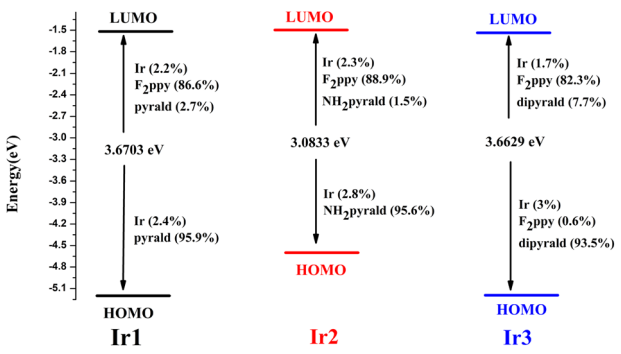

Fig. 4 HOMO and LUMO energy diagram and their compositions with respect to atomic orbitals of different fragments of the complexes (**Ir1–Ir3**).

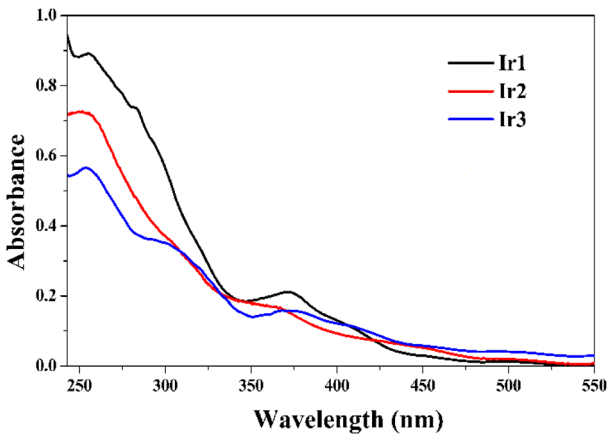

Fig. 5 UV-Vis spectra of complexes (**Ir1–Ir3**) in acetonitrile medium.

complexes, **Ir1–Ir3**. The absorption bands obtained in the range of 345–402 nm were mainly due to HOMO–LUMO transitions. The observed transition found around 371 nm of **Ir1** was broadly suited with a theoretically calculated value of 389.7 nm.

Similarly, the observed transition peaks at 365 and 375 nm of **Ir2** and **Ir3** were well matched with theoretically calculated peaks at 380.9 and 386.2 nm, respectively. Therefore, the electronic spectral peaks in the region 365–375 nm resulted from the transitions of $\pi_{L'}/d_{Ir} \rightarrow \pi^*(F_2ppy)/d_{Ir}$ (L′ = ancillary ligands).

Emission spectra

The photoluminescence spectra were measured at room temperature in an acetonitrile solution (Fig. S14†). Complexes **Ir1** and **Ir3** exhibited emissions in the blue region at 468 and 494 nm, respectively, while **Ir2** showed a red-shifted band at 585 nm. The very identical spectral peak positions of **Ir1** and **Ir3** nullified the substitutional effects of coordinated ancillary ligands on luminescence behaviour. The observation also holds with the identical spin-allowed charge transfer bands at 371 and 375 nm for **Ir1** and **Ir3**, respectively, as mentioned hitherto. In all three complexes, the excited electron in LUMO might have decayed through ligand-centred triplet excited states [^{3}L′LCT (L = F_2ppy, L′ = pyrald/dipyrald)] to the ground state, producing weak phosphorescence.[37] This was also evident from the quantum yield values, as depicted in Table 3.

However, the –NH_2 group of **NH_2pyrald** in **Ir2** had a direct effect on the luminescence spectrum and affected both the spectral shape and the emission maximum. It was found that the –NH_2 group lowered the HOMO–LUMO energy gap and caused a red shift in luminescence behaviour. This could be due to the positive inductive effect of the –NH_2 group, causing an impact on the iridium centre in reference to HOMO–LUMO separation and subsequently resulted lower energy absorption and emission peaks.

The strong luminescence with efficient anticancer activity makes a complex a potential theragnostic agent, *i.e.*, a therapeutic and diagnostic agent, by assessing the mechanism of action of the complexes *via* the cellular uptake, distribution and localisation.[38] The present complexes were found to be weakly luminescent and need structural modification by replacing the pyridine moiety of F_2ppy ligand in **Ir1–Ir3** with imidazole and pyrazole-like aromatic heterocycles, which might improve the emissive behaviour and the theragnostic properties of new compounds.[37]

Electrochemical studies

The electrochemical potentials of all the complexes were studied using cyclic voltammetry in a degassed acetonitrile solution at 298 K. **Ir1** and **Ir3** exhibited two oxidation peaks, while **Ir2** had three anodic responses, as depicted in Fig. 6 and Table 3. The oxidation responses of **Ir1** at 1.17 V, **Ir2** at 0.40 V, 1.42 V and **Ir3** at 1.10 V were attributed to the oxidation of the corresponding coordinated ancillary ligands. The other set of oxidation potentials of three complexes appeared at 1.71 V, 1.87 V and 1.57 V for **Ir1**, **Ir2** and **Ir3**, respectively (Table 3) and were attributed to the Ir(III)–Ir(IV) couples in the respective complexes. For a logical assignment of the anodic peaks of **Ir1–Ir3**, the cyclic voltammograms of **Hpyrald**, **HNH_2pyrald** and **Hdipyrald** in pure form were also recorded in acetonitrile solution (Table 3). Further theoretical calculations revealed

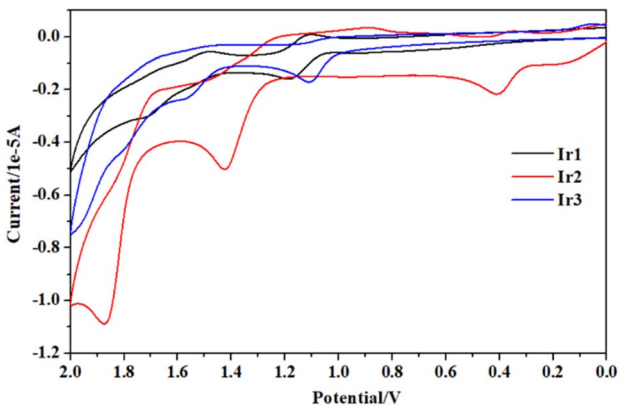

Fig. 6 Cyclic voltammograms of complex **Ir1–Ir3** in acetonitrile solution.

Table 3 Electrochemical and electronic spectral data of complex **Ir1–Ir3**

Complex	Electronic spectral data[a] λ (nm) ($\varepsilon \times 10^4$ M^{-1} cm^{-1})	Photoluminescence data[a]	Quantum yield[b] (Φ)	Electrochemical data[c] [E (V) *vs.* SCE]
Ir1	261 (20.74), 283 (17.07), 371 (4.95), 410 (2.62), 452 (0.61), 501 (0.28)	468 and 494 nm (λ_{ex} = 371 nm)	0.026	1.17[d], 1.71[d]
Ir2	251(36.82), 302 (18.29), 365 (8.44), 450 (2.53), 492 (1.06)	585 nm (λ_{ex} = 365 nm)	0.014	0.40[d], 1.42[d], 1.87[d], −1.33[e]
Ir3	254 (30.81), 293 (19.67), 375 (8.57), 408 (6.17), 500 (2.21)	468 and 494 nm (λ_{ex} = 375 nm)	0.0012	1.10[d], 1.57[d], −1.25[e]
Hpyrald	276, 243			1.24[d], −1.00[e]
HNH_2 pyrald	227, 282			1.15[d], 1.37[d], −1.26[e]
Hdipyrald	230, 265			1.34[d], −1.28[e]

[a] Measured in a degassed acetonitrile solution at room temperature. [b] Quantum yields were determined with respect to [$Ir(ppy)_3$]. [c] Acetonitrile solution (0.1 M TBAP as supporting electrolyte). [d] E_a values. [e] E_c values.

a dominant distribution of HOMO over ancillary ligands; hence, the first oxidation responses of **Ir1–Ir3** were assigned to the oxidation of ancillary ligands. The assignment of Ir(III)–Ir(IV) oxidation responses of complexes was in good agreement with the literature values.[31]

Redox potentials obtained by cyclic voltammetry are often used to calculate the energy levels of HOMO, LUMO and their energy differences. The onset redox potentials were determined assuming the ionisation potentials (IP) of ferrocene value at −5.1 eV.[39] The HOMO–LUMO energy gaps calculated from theoretical calculations, absorption spectra and cyclic voltammograms are presented in Table 4. The optical band gaps were calculated from the absorption peaks at 371 nm, 365 nm and 375 nm for **Ir1–Ir3**, respectively (Tables 3 and S2†) and found in the order of **Ir2** > **Ir1** > **Ir3**. This contradicted the calculated band gaps obtained from TD-DFT calculation, *i.e.* **Ir1** > **Ir3** > **Ir2**. Therefore, the observed trend of HOMO–LUMO energy gaps for complexes **Ir1** and **Ir3** using both optical and theoretical methods was found to be the same, while **Ir2** stands out with a deviation. Electrochemical band gaps calculated from the onset oxidation and reduction potentials for **Ir2** and **Ir3** were found to have values of 2.75 eV and 2.35 eV, respectively, but the electrochemical band gap for **Ir1** could not be evaluated owing to the absence of a reduction response.

Anticancer studies

Antiproliferative assay. The *in vitro* antiproliferative activity of **Ir1–Ir3** complexes was evaluated using the MTT assay of human breast cancer cell lines (MDA-MB 231), colon cancer cell line (HT-29) and human glioblastoma cell lines (LN-229) for 48 hours. The results revealed that the complexes efficiently inhibit the proliferation of three cancer cells after 48 hours of incubation. The half maximal inhibitory concentration values (IC_{50}) of the complexes were calculated, as presented in Table 5. Among the three iridium complexes, **Ir2** was found to exhibit the highest cell cytotoxicity towards all three cancer cells with IC_{50} values ranging from 8.6 to 12.3 μM, which were comparable to the 50% inhibitory concentration of cisplatin (8.3 to 10.3 μM) (Table 5). **Ir3** showed the least cytotoxic effects on cancer cells with a high range of IC_{50} values, *i.e.* 21.3 to 31.32 μM (Table 5),

Table 4 Redox potentials, HOMO and LUMO energies, and electrochemical band gaps (E_g) of **Ir1–Ir3**

	Ir1	Ir2	Ir3
E_{ox}	1.17	1.42	1.10
E_{red}		−1.33	−1.25
HOMO[a] (CV)	−6.27	−6.52	−6.20
LUMO[b] (CV)		−3.77	−3.85
HOMO(DFT)	−5.19	−4.59	−5.19
LUMO(DFT)	−1.52	−1.50	−1.53
$E_{g(CV)}$[c] [eV]		**2.75**	**2.35**
$E_{g(opt)}$[d] [eV]	**3.34**	**3.39**	**3.30**
$E_{g(DFT)}$ [eV]	**3.67**	**3.08**	**3.66**

[a] HOMO = −5.1 − E_{ox}. [b] LUMO = −5.1 − E_{red}. [c] $E_{g(CV)} = E_{ox(onset)} - E_{red(onset)}$. [d] $E_{g(opt)} = 1240/\lambda_{abs}$.

Table 5 IC_{50} (μM) values of the complexes toward selected cancer cell lines after 48 hours

Complex	MDA-MB 231	HT-29	LN 229
Ir1	11.30 ± 0.95	14.20 ± 1.21	16.23 ± 1.20
Ir2	8.60 ± 0.98	10.45 ± 1.71	12.30 ± 1.02
Ir3	21.30 ± 1.30	27.30 ± 2.87	31.32 ± 3.31
Cisplatin	8.30 ± 0.87	9.50 ± 1.10	10.30 ± 1.45

and moderate toxicity was observed for **Ir1** towards the human cancer cells (IC_{50} = 11.3 to 16.23 μM). The observed difference in the antiproliferation activities of **Ir1–Ir3** was ascribed to the structural variation in ancillary ligands in the complexes. Thus, the highest cell cytotoxicity in **Ir2** may be attributed to potential interactions of the $-NH_2$ group present in the coordinated **NH_2pyrald** ligand with subcellular organelles.[40,41]

Intracellular ROS measurement. To further elucidate the mechanism of action, cyclometallated complex **Ir1–Ir3** was evaluated owing to their ability to induce apoptosis. The total ROS assay was performed using the fluorescent probe DCFH-DA (2′,7′-dichlorofluorescein-diacetate). The reactive oxygen species cause oxidation in DCFH-DA to produce fluorophore 2′,7′-dichlorofluorescein (DCF). Thus, the mean DCF fluorescence intensity increases with an increase in drug concentration within the cancer cells, indicating the production of ROSs (Fig. 7). The results revealed that **Ir1–Ir3** significantly increased the intracellular ROS levels in cancer cells (Fig. 7). This increase in ROS production may contribute to the cytotoxic effects of complexes, such as oxidative stress, which is known to trigger apoptotic signalling pathways.[42] **Ir2** was found to produce more ROS compared with the other two iridium complexes in all three cancer cell lines (Fig. 7). The least reactive oxygen species was generated in the case of **Ir3**. The data obtained in the ROS generation studies were in good agreement with the cell viability assay test.

Cell migration study. Cellular migration and invasion play a crucial role in spreading cancer cells from one organ to another through metastasis and increasing the mortality risk.[43] Cell migration assay in LN-229 cells was performed to check potent cell migration activity. The migratory potential of the LN-229 cell lines was significantly inhibited by the addition of iridium complex **Ir1–Ir3** to the corresponding cell lines (Fig. 8). Among all the complexes, **Ir2** was found to inhibit cell migration most significantly (Fig. 8) and **Ir3** showed the least cell migration inhibition. **Ir2** attacked cells more prominently through $-NH_2$ group present in the ancillary moiety, suppressing dynamic instability and showing the most significant result.[40,41]

Colony formation assay. A colony formation assay was employed to assess the long-term effects of the iridium complexes on the proliferative capacity of cancer cells. The results showed that the complexes effectively suppressed the colony-forming ability of HT-29 cells in a dose-dependent manner, suggesting their potential to inhibit tumor growth. All the complexes showed inhibition in colony formation with respect to the control. **Ir2** was found to inhibit colony formation

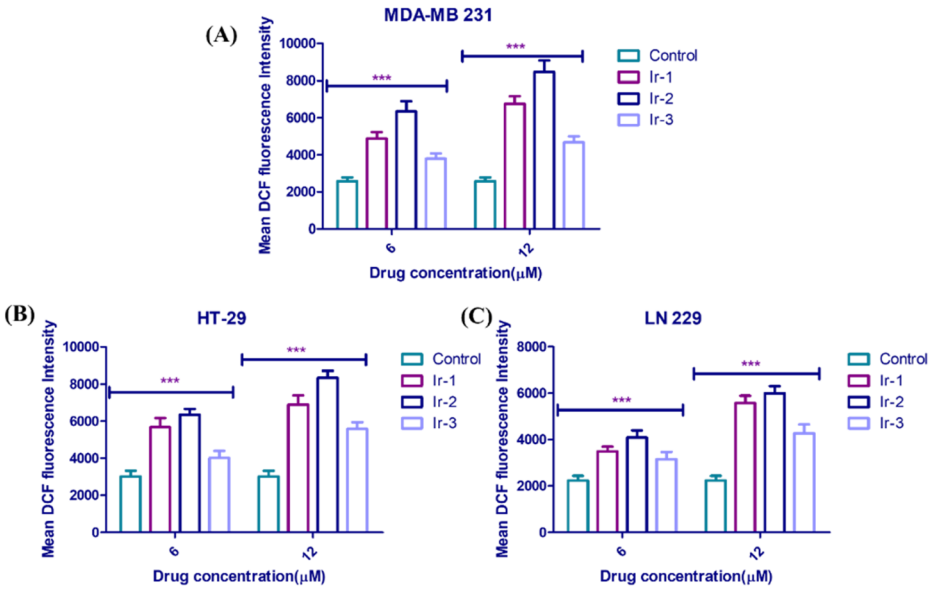

Fig. 7 Intracellular ROS levels were assessed in (A) MDA-MB 231, (B) HT-29, and (C) LN-229 cells following treatment with **Ir1–Ir3** using a DCFH-DA fluorescence assay. Cells were incubated with 6 and 12 μM of the complexes for 48 hours, and ROS levels were quantified by measuring fluorescence intensity and expressed as mean fluorescence intensity. Data were expressed as mean ± SD. ($n = 3$), ***$P < 0.01$ *versus* control.

with reduced colony number and size, most significantly compared to the other two complexes, **Ir1** and **Ir3** (Fig. 9). Similarly, **Ir3** showed the least inhibiting activity compared to the others in the colony formation assay. There was no significant decrease in colony formation in the case of **Ir3**, while **Ir1** showed moderate inhibitory activity.

Immunocytochemistry. Immunocytochemistry analysis revealed that the iridium complexes induced the upregulation and nuclear localization of the tumor suppressor protein p53, as well as the activation of cleaved caspase, a key mediator of apoptosis. Complex **Ir2** showed more nuclear localisation of p53 and activation of cleaved caspase 3 and also a change in the cell morphology, while **Ir3** showed the least result (Fig. 10). These findings suggest that the complexes may induce apoptosis in cancer cells through the p53-dependent pathway. These findings align with previous studies on the ability of iridium-based complexes to modulate the expression and activity of apoptosis-related proteins to elicit anticancer effects.[40]

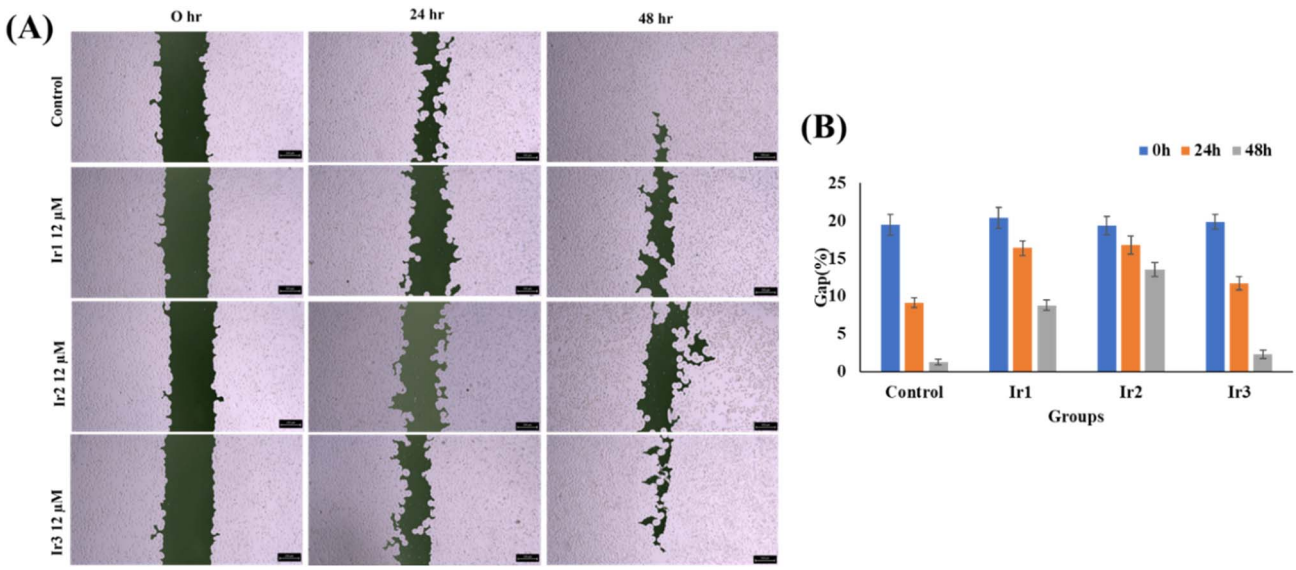

Fig. 8 Cell migration assay of LN-229 cells treated with or without **Ir1–Ir3** for 24 and 48 hours. (A) Representative images of cell migration at 0 hours, 24 hours and 48 hours post-treatment, comparing untreated control and complex **Ir1–Ir3** treated cells. (B) Quantification of the migration rate, expressed as the percentage of gap closure relative to the control. Data represent mean ± SD from three independent experiments.

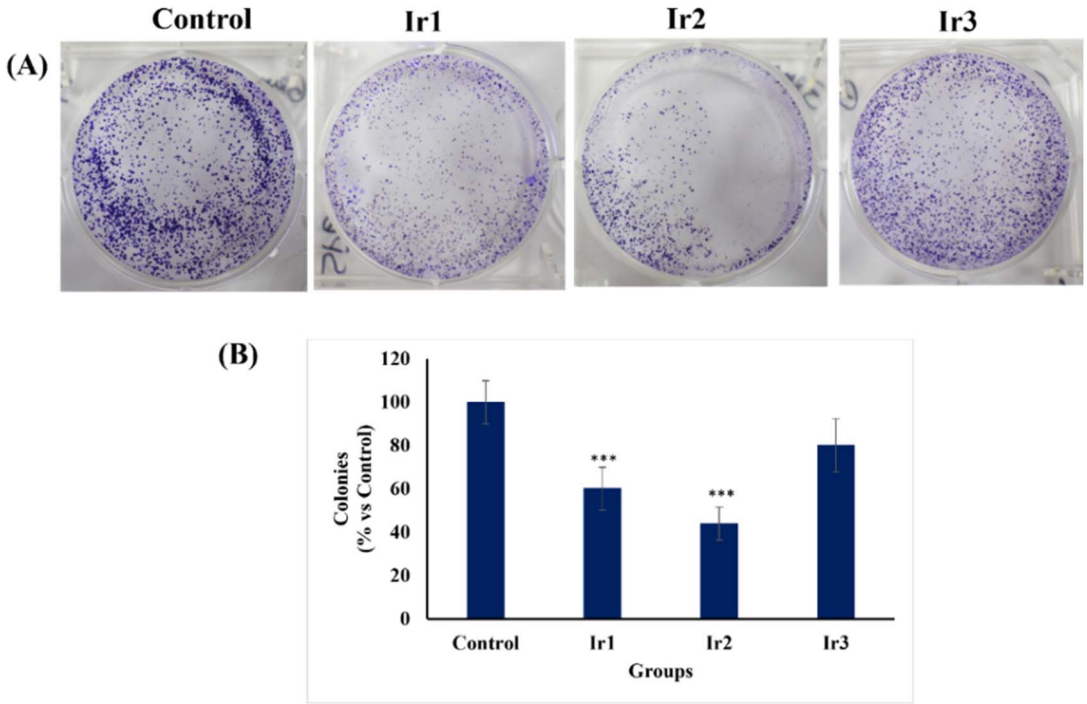

Fig. 9 Colony formation was assessed in HT-29 cells following treatment with complex **Ir1–Ir3** using a clonogenic assay. (A) Representative images of colonies formed in untreated control and **Ir1–Ir3** treated groups after 14 days. (B) Quantification of colony formation, expressed as the percentage of colonies relative to the control. All values are expressed as the mean ± SD ($n = 3$), ***$P < 0.01$ *versus* control.

Apoptosis study. The AO/PI staining assay confirmed that the **Ir1–Ir3** complexes effectively induced apoptosis in cancer cells, as evidenced by the increased percentage of cells undergoing early and late apoptosis (Fig. 11). This study further supported the superior anticancer efficacy of complex **Ir2** with both early and late apoptosis and high cell morphology irregularity after treatment. Complex **Ir1** mostly induced early apoptosis with the maximum observation of greenish yellow with orange cancer cells compared to red-orange, and the least activity was observed for complex **Ir3**.

Experimental

Materials and synthesis of complexes

$IrCl_3 \cdot xH_2O$, 2-pyridinealdoxime (**Hpyrald**), 2-(2,4-difluorophenyl)pyridine (**HF_2ppy**), and di-2-pyridyl ketoxime (**Hdipyrald**) were obtained from Merck and used without further purification. Pyridine-2-amidoxime (**HNH_2pyrald**) was purchased from BLD Pharm, India. MTT [3-(4,5-dimethylthiazol-2-yl)-2,5-diphenyltetrazoliumbromide], acridine orange and ethidiumbromide were purchased from Merck USA. The human cancer cell lines MDAMB, HT-29 and LN-229 were obtained from CSIR-National Chemical Laboratory, Pune, India. All chemicals for cell culture, such as DMEM (Dulbecco's modified Eagle's medium), fetal bovine serum (FBS) and trypsin–EDTA were purchased from Himedia Laboratories Pvt. Ltd, Mumbai, India. All the solvents were dried following reported methods[44] before use. The chloro-bridged dimer $[Ir(F_2ppy)_2(\mu\text{-}Cl)_2Ir(F_2ppy)_2]$ (SM1) was prepared from $IrCl_3 \cdot xH_2O$ using the method described by Nonoyama.[45]

Synthesis of $[Ir(F_2ppy)_2(pyrald)]$ (Ir1), $[Ir(F_2ppy)_2(NH_2pyrald)]$ (Ir2) and $[Ir(F_2ppy)_2(dipyrald)]$ (Ir3)

Iridium complex **Ir1–Ir3** was synthesised following the synthetic procedure proposed by Nonoyama.[45] In a typical preparation of **Ir1**, the dichloro-bridged dimer, $[(F_2ppy)_2Ir(\mu\text{-}Cl)_2Ir(F_2ppy)_2]$ **(SM1)** (200 mg, 0.16 mmol) reacted with pyridine-2-aldoxime (**Hpyrald**) (49 mg, 0.40 mmol) and Et_3N (0.056 ml, 0.40 mmol) in 30 ml ethanol under reflux condition under dinitrogen atmosphere for 18 hours (Scheme S1†). The resulting mixture was evaporated in a water bath. The impure mixture thus obtained was applied to a neutral aluminium oxide column and eluted with acetonitrile to isolate a yellow band. The evaporation of the column-separated solution resulted in a yellow solid with a 90% yield (205 mg).

$[Ir(F_2ppy)_2(pyrald)]$ (Ir1). IR data (cm^{-1}, ATR): 1733(w), 1600(s), 1569(w), 1557(m), 1472(s), 1416(w), 1403(s), 1330(m), 1292(m), 1265(w), 1243(s), 1146(s), 1102(s), 1068(w), 1042(m), 983(s), 839(w), 824(s), 755(w), 749(s), 711(m), 676(s), 649(w), 610(w), 568(s), 525(s), 456(w).

^{1}H NMR data (400 MHz, DMSO-d_6, ppm): δ 8.37 (d, J = 5.5 Hz, 1H), 8.24 (d, J = 7.7 Hz, 3H), 8.03 (t, J = 7.8 Hz, 2H), 7.77 (t, J = 6.8 Hz, 1H), 7.65 (d, J = 6.2 Hz, 1H), 7.51 (d, J = 8.8 Hz, 1H), 7.48–7.42 (m, 1H), 7.39 (d, J = 4.9 Hz, 1H), 7.36–7.29 (m, 1H), 7.09–7.01 (m, 1H), 6.89–6.79 (m, 1H), 6.79–6.67 (m, 1H), 5.66 (d, J = 8.3 Hz, 1H), 5.44 (d, J = 9.6 Hz, 1H).

^{19}F NMR data (377 MHz, DMSO-d_6, ppm): δ −107.76, −108.97, −109.51, −110.97.

ESI-MS for $[Ir(F_2ppy)_2(pyrald)]$ (**Ir1**): theoretical mass for $C_{28}H_{17}N_4F_4OIr$, 694.0968; found 694.7900.

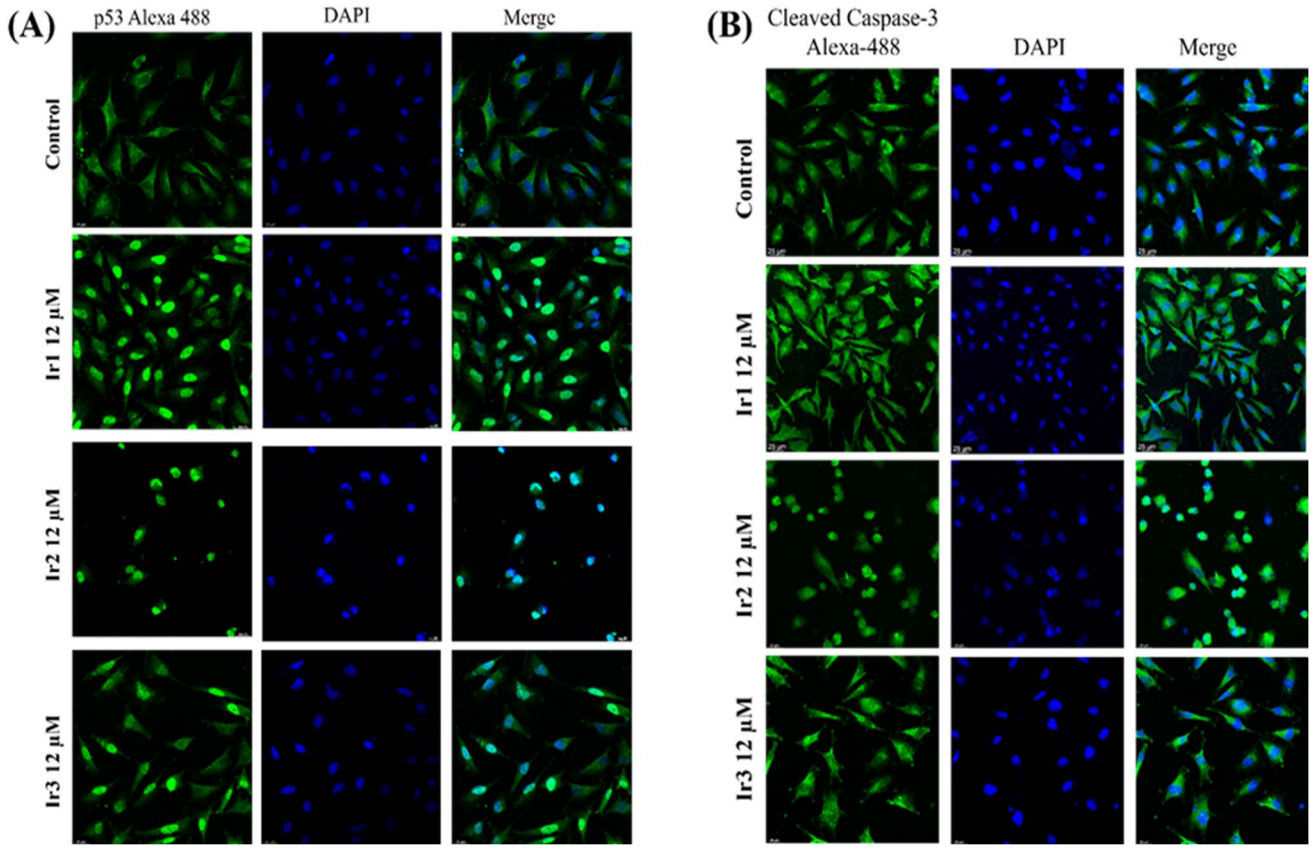

Fig. 10 (A) Iridium complexes induce nuclear translocation of p53 and (B) activation of cleaved caspase3. Confocal microscopy images of LN 229 cells treated with 12 μM **Ir1–Ir3** for 48 hours and stained with anti-p53 and cleaved caspase-3 primary antibodies, followed by incubation with the Alexa-488-conjugated secondary antibody and DAPI for nuclear staining.

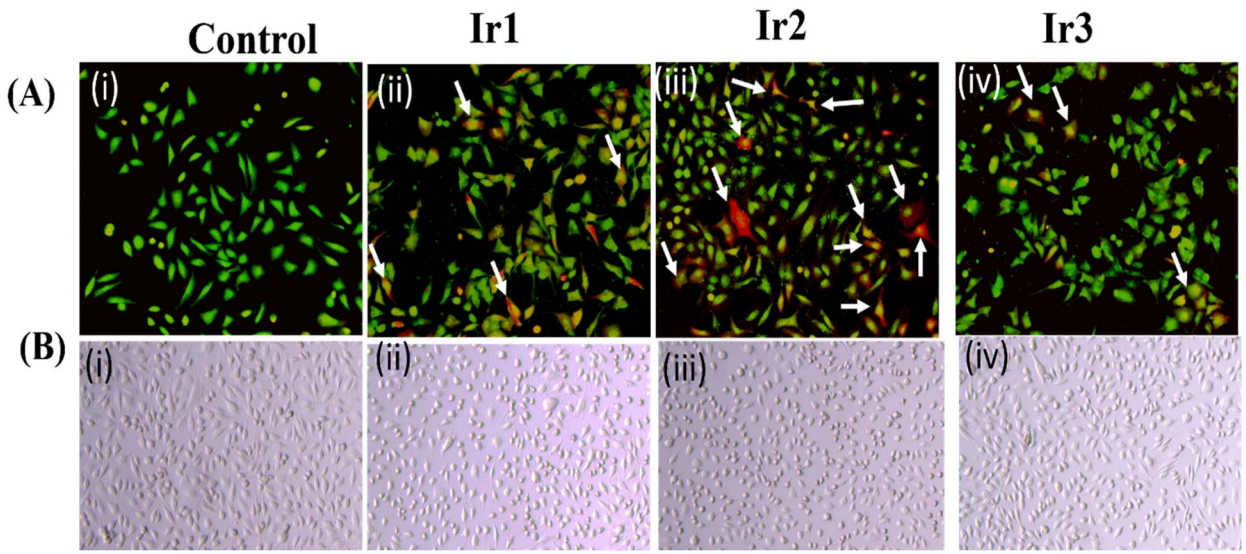

Fig. 11 (A) Investigation of apoptosis induction in **Ir1–Ir3** treated with LN 229 cells by fluorescence microscope with acridine orange and propidium iodide: (i) control, (ii) **Ir1**, (iii) **Ir2** and (iv) **Ir3**. Untreated control cells emitted green fluorescence. Treated cells showed greenish-yellow with orange nuclei at the early apoptotic phase (pointed as white arrow), and the cells turned red-orange at the late apoptosis phase (pointed as white arrow). (B) Change in cell shape with **Ir1–Ir3** treatment: (i) control, (ii) **Ir1**, (iii) **Ir2**, and (iv) **Ir3**. The LN-229 cells were treated with or without **Ir1–Ir3** (12 μM) for 48 hours. Bright-field images showed the change in morphology after treatment, and cells acquired with poorly defined and irregular cell morphology with iridium complex treatment. Magnification: ×10 and ×20.

Elemental analysis: anal. calcd for $C_{28}H_{17}N_4F_4OIr$: C, 48.48; H, 2.47; N, 8.08. Found C, 49.69; H, 3.12; N, 8.98.

[Ir(F_2ppy)$_2$(NH_2pyrald)] (Ir2). Ir2 was prepared following the very same procedure described for **Ir1**. The crude product obtained from the reaction mixture was purified on an Al_2O_3 column by eluting it with an acetonitrile and hexane mixture (4 : 1, v/v). The complex was isolated as a yellow powder with a 64.7% yield.

IR data (KBr, cm^{-1}): 3063(w), 1603(s), 1571(w), 1558(w), 1474(s), 1440(m), 1400(s), 1360(m), 1288(s), 1247(s), 1162(s), 1100(s), 1043(w), 985(s), 828(s), 785(m), 755(m), 700(m), 668(m), 568(w), 526(w), 418(w).

^{1}H NMR data (400 MHz, DMSO-d_6, ppm): δ 8.34 (d, J = 4.8 Hz, 1H), 8.28–8.18 (m, 2H), 8.01 (t, J = 7.9 Hz, 2H), 7.92 (t, J = 7.8 Hz, 1H), 7.72 (d, J = 7.5 Hz, 1H), 7.58 (d, J = 5.1 Hz, 1H), 7.52–7.39 (m, 2H), 7.30 (t, J = 6.0 Hz, 1H), 7.22–7.10 (m, 1H), 6.83 (ddd, J = 12.1, 9.5, 2.3 Hz, 1H), 6.73 (ddd, J = 12.2, 9.5, 2.3 Hz, 1H), 5.81 (s, 2H), 5.65 (dd, J = 8.1, 2.4 Hz, 1H), 5.46 (dd, J = 8.9, 2.4 Hz, 1H).

^{19}F NMR data (377 MHz, DMSO-d_6, ppm): δ −107.73, −109.03, −109.44, −111.11.

ESI-MS for [Ir(F_2ppy)$_2$(NH_2pyrald)] (**Ir2**): theoretical mass for $C_{28}H_{19}N_5F_4OIr$ $[Ir2H]^+$, 710.1077; found 710.0981.

Elemental analysis: anal. calcd for $C_{28}H_{18}N_5F_4OIr$: C, 47.45; H, 2.56; N, 9.88. Found C, 48.06; H, 3.01; N, 10.42.

[Ir(F_2ppy)$_2$(dipyrald)] (Ir3). Ir3 was also prepared following the same procedure described for complex **Ir1**.

The crude product was purified on an Al_2O_3 column by eluting with an acetone : methanol (1 : 1, v/v) mixture. The greenish-yellow coloured powder was obtained with a yield of 65%.

IR data (KBr, cm^{-1}): 3063(w), 1603(s), 1571(w), 1558(w), 1474(s), 1440(m), 1400(s), 1360(m), 1288(s), 1247(s), 1162(s), 1100(s), 1043(w), 985(s), 828(s), 785(m), 755(m), 700(m), 668(m), 568(w), 526(w), 418(w).

^{1}H NMR data (400 MHz, DMSO-d_6, ppm): δ 8.65 (d, J = 4.8 Hz, 1H), 8.46 (d, J = 4.9 Hz, 1H), 8.27 (t, J = 8.3 Hz, 2H), 8.05 (t, J = 7.8 Hz, 2H), 7.84–7.69 (m, 4H), 7.58–7.45 (m, 3H), 7.41–7.29 (m, 2H), 7.17–7.11 (m, 1H), 6.91–6.82 (m, 1H), 6.78–6.67 (m, 1H), 5.70 (dd, J = 8.1, 2.3 Hz, 1H), 5.46 (dd, J = 8.8, 2.4 Hz, 1H).

^{19}F NMR data (377 MHz, DMSO-d_6, ppm): δ −107.64, −109.09, −109.47, −111.06.

ESI-MS for [Ir(F_2ppy)$_2$(dipyrald)] (**Ir3**): theoretical mass for $C_{33}H_{21}N_5F_4OIr$ $[Ir3H]^+$, 772.1233; found 772.1311.

Elemental analysis: anal. calcd for $C_{33}H_{20}N_5F_4OIr$: C, 51.42; H, 2.62; N, 9.09. Found C, 52.26; H, 2.98; N, 9.78.

Physical measurements

The FT-IR spectra of the complexes were recorded using a Shimadzu IR Afinity-1S spectrophotometer with a KBr pallet. A Bruker 700 MHz spectrometer was used to measure ^{1}H and ^{19}F NMR data for all the complexes using a dry DMSO-d_6 solvent. The Thermo Finnigan Flash EA1112 series instrument was used for the elemental (C, H, N) analysis of the iridium complexes. An Agilent Carry 100 UV-Vis spectrophotometer instrument was used to record the absorption spectra of all the complexes. A Shimadzu RF 6000 fluorescence spectrometer was used to obtain the photoluminescence spectra. Cyclic voltammograms were recorded on CH Instrument model CHI760E to observe the oxidation and reduction potentials of the iridium complexes. The redox properties were studied under a dinitrogen atmosphere in an acetonitrile medium at room temperature using $[(n\text{-}C_4H_9)_4N]ClO_4$ (TBAP) as a supporting electrolyte. The Pt-disk electrode was used as the working electrode, while Pt-wire and saturated calomel (SCE) were used as the reference and auxiliary electrodes, respectively. All the mass spectra were recorded using a Bruker micro TOF-QII mass spectrometer.

Crystal structure determination

The X-ray quality single crystal of [Ir(F_2ppy)(pyrald)] (**Ir1**) was obtained upon slow evaporation of a methanol–toluene mixture at room temperature. A suitable single crystal was chosen and mounted on a Rigaku CCD X-ray diffractometer. The X-ray data were collected at 296 K using a microfocus sealed X-ray tube with Cu-Kα (λ = 1.54184 Å) as an X-ray source. The obtained data were refined and reduced through the CrysAlisPro software for further processing. The structure was solved using SHELXT software and refined on F^2 by applying a full-matrix least-squares method with the SHELXL programme assembled in Wingx software. The thermal parameters of all the non-hydrogen atoms were refined anisotropically, and hydrogen atoms were added to the atoms at an idealised position using the riding model. The structure was crystallised with one molecule of methanol. The final crystallographic data were submitted to CCDC with deposition numbers 2377820 and 2377821. The different refinement parameters along with selected bond lengths and angle parameters are listed in Tables 1 and S3,† respectively. The thermal ellipsoid plot, as depicted in Fig. 3, was obtained from the ORTEP 3 programme.

Computational methods

The ORCA programme was used for the time-dependent density functional theory (TD-DFT) calculation of complex **Ir1–Ir3**.[46] The geometries of all the complexes were optimised in the gas phase prior to theoretical calculations. The hybrid B3LYP-D3/def2-TZVP level of theory was used for TD-DFT calculations.[47] Two different basis sets were employed to treat the non-metallic and metallic atoms present in complexes. The Basis LanL2DZ set was used to treat the iridium atom,[48] and 6-31G** basis set was used for the treatment of non-metallic atoms, such as C, N, H and F, present in ligand frameworks.[49,50] Hessian indices were used as a tool to examine the stationary states. TD-DFT calculations of all the complexes were performed at the gas phase optimized geometry using the SMD continuum solvation model for acetonitrile stated by Truhlar and Cramer.[51]

Anticancer study

Cell culture. The MDA-MB 231, HT-29 and LN-229 cancer cell lines were cultured using DMEM with 10% FBS, 1% L-glutamine and 1% penicillin streptomycin at 37 °C in a humidified, 5% CO_2 incubator (Galaxy 170 R, Eppendorf, Germany).

Cell viability assay. The MTT (3-(4,5-dimethylthiazol-2-yl)-2,5-diphenyltetrazolium bromide) assay was performed to evaluate the cytotoxic potential of **Ir1–Ir3** against a panel of cancer cell lines, including MDA-MB 231, HT-29, and LN 229.34. Briefly, these cells were seeded into 96-well plates (NEST Scientific Inc., USA) at a density of 3000 cells per well and incubated in a growth medium at 37 °C for 24 hours to facilitate attachment. The following day, the cells were exposed to varying concentrations of **Ir1–Ir3** dissolved in DMSO (with DMSO concentration kept below 0.01%) and incubated for 48 hours. Cells treated with medium alone served as controls. After the incubation period, the medium was replaced with 100 μl MTT (5 mg ml^{-1}) containing media, and the cells were incubated for an additional 4 hours. The resulting formazan crystals were dissolved in DMSO, and their absorbance was measured at 570 nm using an ELISA plate reader (BioTek Epoch, USA).

Intracellular ROS measurement. The total reactive oxygen species (ROS) assay was performed to assess the ability of the iridium complexes (**Ir1–Ir3**) to induce oxidative stress in cancer cells. The generation of ROS was evaluated using the DCFH-DA fluorescent dye protocol with minor modifications.[52] Briefly, MD-MB 231, HT-29, and LN 229 cells (1×10^5 cells per well) were seeded into 6-well plates (NEST Scientific Inc., USA) containing growth medium and incubated overnight at 37 °C to allow for cell attachment. The following day, the cells were exposed to varying concentrations of **Ir1–Ir3** dissolved in DMSO (with a DMSO concentration of less than 0.01%) and incubated at 37 °C for 48 hours. Cells treated with the growth medium alone served as controls. After the incubation period, the cells were washed twice with PBS and incubated with 10 μM DCFH-DA for 30 minutes. Subsequently, the excess dye was removed by washing with PBS. The cells were then lysed, and the fluorescence intensity of the lysates was measured using a fluorescence spectrophotometer (Agilent) with an excitation wavelength of 488 nm and an emission wavelength of 530 nm.

Cell migration assay. To investigate the migratory potential of the LN 229 cancer cell line in response to **Ir1–Ir3** complexes, a wound-healing assay was performed.[53] Briefly, LN 229 cells were seeded into 6-well plates (NEST Scientific Inc., USA) at a density of 1×10^5 cells per well and allowed to form a confluent monolayer overnight at 37 °C with 5% CO_2. After 24 hours, a scratch was introduced into the cell monolayer using a 200 μl pipette tip. The wells were then gently washed with PBS to remove any cellular debris generated during scratch formation. The cells were then treated with 12 μM of **Ir1–Ir3** for 48 hours, while the control cells received only the culture medium. Photographic images of the scratch were captured at the initial point in time and after 24 and 48 hours of incubation using an inverted microscope equipped with a digital camera. The open, cell-free areas created by the scratch were analyzed using TScratch software, and the migration rate was quantified as the percentage reduction in the wound area over time, as the cells migrated to close the scratch.

Colony formation assay. To assess the long-term effects of **Ir1–Ir3** complexes on the clonogenic potential of HT-29 cells, a colony formation assay was conducted.[54] Specifically, 1000 cells were seeded per well in a six-well plate (NEST Scientific Inc., USA) and allowed to adhere for 4 hours. Subsequently, the cells were exposed to 12 μM of **Ir1–Ir3**, while medium-treated cells served as controls. The cells were then incubated at 37 °C with 5% CO_2 for 14 days, with the culture medium replenished every 2 days. After the 14-days incubation period, the cells were fixed with 70% ethanol and stained with 0.5% crystal violet, and the colony formations were analyzed. A cell colony was defined as a cluster of at least 50 cells, and the colonies were quantified using ImageJ software (National Institutes of Health, Bethesda, Maryland, USA).

Immunolocalization analysis. Immunocytochemistry was employed to investigate the impact of **Ir1–Ir3** on the expression of key apoptosis-related proteins, including p53 and cleaved caspase-3.[55] Briefly, LN 229 cells were seeded onto coverslips (NEST Scientific Inc., USA) at a density of 1×10^4 cells per coverslip and incubated in growth medium at 37 °C for 24 hours to facilitate cell attachment. The following day, the cells were exposed to 12 μM of **Ir1–Ir3** complexes for 48 hours, with medium-treated cells serving as controls. After the treatment period, the cells were thoroughly washed with PBS, fixed with 4% paraformaldehyde and subjected to blocking with 5% BSA. Subsequently, the cells were incubated for 3 hours with primary antibodies specific for p53 and cleaved caspase-3 (Santa Cruz Biotechnology Inc., Dallas, TX, USA) at a dilution of 1:150. Goat anti-rabbit IgG-Alexa-488 secondary antibodies (Invitrogen, USA) were then used to incubate the cells at a dilution of 1:100 for 1 hour. DAPI was employed to stain the cell nuclei. The expression levels of these apoptotic markers were analyzed using confocal microscopy (Stellaris 5, Leica Confocal Microscope).

Assessment of apoptosis (propidium iodide/acridine orange assay). Propidium iodide/acridine orange (PI/AO) dual staining was used to measure the apoptotic rates in the control and iridium complex-treated LN 229 cancer cells.[56] Briefly, LN-229 cells were seeded onto coverslips (NEST Scientific Inc., USA) at a density of 1×10^4 cells per coverslip and incubated in a growth medium at 37 °C for 24 hours to facilitate cell attachment. The following day, the cells were exposed to 12 μM of **Ir1–Ir3** complexes for 48 hours, with medium-treated cells serving as controls before AO/PI staining. After the incubation period, the cells were washed twice with PBS and incubated with AO/PI staining (10 μM AO/10 μM PI) for 30 minutes. Subsequently, the excess dye was removed by washing with PBS. Photographs were taken directly under a fluorescent microscope (Olympus BX63, Olympus Corp., Tokyo, Japan).

Statistical analysis. All the experiments were repeated a minimum of three times. Data are presented as mean ± standard deviation, and analyzed by one-way ANOVA with Tukey's test applied post hoc for comparisons of means (Prism 5.0, GraphPad Software Inc., CA, USA). The value of $***P < 0.01$ indicated significant differences.

Conclusions

Three bis-heteroleptic Ir(III)–F_2ppy complexes (**Ir1–Ir3**) were designed and synthesised, aiming to explore the ortho C–H bond activation potential inherited within the pyridine-2-

aldoxime and its two derivatives. However, the ortho C–H bond activation phenomenon was found to be absent in the present complexes, which was also confirmed by the single crystal X-ray structures of **Ir1** and **Ir3**. The molecular structures displayed distorted octahedral geometry with the usual C^N coordination of F_2ppy ligands around the Ir(III) centres and an innocent character of aldoxime ligands. All the complexes exhibited very weak luminescence in the solution medium. Anticancer studies with MDAMB, HT-29 and LN 229 cancer cells revealed the cytotoxic nature of all the iridium complexes. The complexes induce oxidative stress by generating reactive oxygen species, which were ultimately associated with the induction of apoptosis in cancer cells. The suppression of colony formation and cell migration by the iridium complexes further underscores their potential to inhibit key cellular processes essential for tumour growth and metastasis. The observed upregulation and nuclear localization of crucial tumour suppressor protein p53 and the activation of caspase-3, a hallmark of apoptosis, suggested that complex **Ir1–Ir3** may induce programmed cell death through the p53-dependent pathway. All the biological studies supported the superior anticancer activity of complex **Ir2** among the three complexes, and **Ir3** was found to be the least effective.

Data availability

The data supporting this article have been included as part of the ESI.†

Conflicts of interest

There are no conflicts to declare.

Acknowledgements

The financial support from the Science and Technology Department, Govt. of Odisha (Grant No. 27562800512017/201288/ST/Bhubaneswar, dt. 24.02.2018) and OSHEC MRIP-2024-Chemistry (Grant No. 305/249/OSHEC, dt. 17.03.2025) is gratefully acknowledged. The work is also supported by the World Bank-Odisha Higher Education Programme for Excellence and Equity (WB-OHEPEE, Letter No-Dev-I/1113/PV/9072/2022, dt. 31.3.2022), DST-FIST program of Govt. of India (SR/FST/CSI/-275/2016 (C) dt. 01.02.2018), RUSA 2.0 and COE in Advanced Materials and Applications of Utkal University.

References

1 Y. Lan, D. Liu, J. Li, H. Wan and Y. Mei, 2-Phenylpyridine-Based Phosphorescent Ir(III) Complexes for Highly Efficient Greenish-Blue Organic Light-Emitting Diodes with EQEs up to 33.5%, *Dyes Pigm.*, 2023, **210**, 111032.

2 V. Chandrasekhar, B. Mahanti, M. D. Pandey and R. S. Narayanan, Cyclometalated Ir(III) Complex as a Metalloligand and a Selective Cu(II) Sensor: Synthesis and Structural Characterization of a Heterometallic Tetranuclear Ir(III)/Cu(II) Complex, *ACS Omega*, 2018, **3**, 2786–2792.

3 S. Wu, Y. Wang, Y. Zhao, R. Wang, M. Hailin and T. Yu, Synthesis and Luminescence Properties of Two Ir(III) Complexes Containing Styrene-Modified Phenylpyridine Ligands, *New J. Chem.*, 2021, **45**(6), 3311–3318.

4 A. F. Henwood and E. Zysman-Colman, Luminescent Iridium Complexes Used in Light-Emitting Electrochemical Cells (LEECs), *Top. Curr. Chem.*, 2016, **374**(4), 36.

5 J. H. Seo, Y. K. Kim and Y. Ha, Efficient Blue-Green Organic Light-Emitting Diodes Based on Heteroleptic Tris-Cyclometalated Iridium(III) Complexes, *Thin Solid Films*, 2009, **517**(5), 1807–1810.

6 G. Y. Park, Y. Kim and Y. Ha, Iridium Complexes Containing Three Different Ligands as White OLED Dopants, *Mol. Cryst. Liq. Cryst.*, 2006, **462**(1), 179–188.

7 R. Davidson, Y.-T. Hsu, M. A. Fox, J. A. Aguilar, D. Yufit and A. Beeby, Tuning Emission Lifetimes of Ir(C^N)$_2$(Acac) Complexes with Oligo(Phenyleneethynylene) Groups, *Inorg. Chem.*, 2023, **62**(6), 2793–2805.

8 M. R. Schreier, X. Guo, B. Pfund, Y. Okamoto, T. R. Ward, C. Kerzig and O. S. Wenger, Water-Soluble Tris(Cyclometalated) Iridium(III) Complexes for Aqueous Electron and Energy Transfer Photochemistry, *Acc. Chem. Res.*, 2022, **55**(9), 1290–1300.

9 B. Joshi and M. Shivashankar, Recent Advancement in the Synthesis of Ir-Based Complexes, *ACS Omega*, 2023, **8**(46), 43408–43432.

10 H. Zhang, L. Tian, R. Xiao, Y. Zhou, Y. Zhang, J. Hao, Y. Liu and J. Wang, Anticancer Effect Evaluation *in Vitro* and *in Vivo* of Iridium(III) Polypyridyl Complexes Targeting DNA and Mitochondria, *Bioorganic Chem.*, 2021, **115**, 105290.

11 N. Neelambaran, S. Shamjith, V. P. Murali, K. K. Maiti and J. Joseph, Exploring a Mitochondria Targeting, Dinuclear Cyclometalated Iridium (III) Complex for Image-Guided Photodynamic Therapy in Triple-Negative Breast Cancer Cells, *ACS Appl. Bio Mater.*, 2023, **6**(12), 5776–5788.

12 A. Sharma S, S. P, N. Roy and P. Paira, Advances in Novel Iridium (III) Based Complexes for Anticancer Applications: A Review, *Inorganica Chim. Acta*, 2020, **513**, 119925.

13 Z. Liu and P. J. Sadler, Organoiridium Complexes: Anticancer Agents and Catalysts, *Acc. Chem. Res.*, 2014, **47**(4), 1174–1185.

14 T. Yang, M. Zhu, M. Jiang, F. Yang and Z. Zhang, Current Status of Iridium-Based Complexes against Lung Cancer, *Front. Pharmacol.*, 2022, **13**, 1025544.

15 L. Xie, L. Shi, K. Xiong, R. Guan, Y. Chen, J. Long, L. Ji and H. Chao, Synthesis, Subcellular Localization and Anticancer Mechanism Studies of Unsymmetrical Iridium(III) Complexes, *Eur. J. Inorg. Chem.*, 2023, **26**(15), e202300001, DOI: 10.1002/ejic.202300001.

16 Q.-Y. Yi, D. Wan, B. Tang, Y.-J. Wang, W.-Y. Zhang, F. Du, M. He and Y.-J. Liu, Synthesis, Characterization and Anticancer Activity *in Vitro* and *in Vivo* Evaluation of an Iridium (III) Polypyridyl Complex, *Eur. J. Med. Chem.*, 2018, **145**, 338–349.

17 Y. Wu, J. Liu, M. Shao, P. Zhang, S. Song, G. Yang, X. Liu and Z. Liu, Cyclometalated Iridium(III) Dithioformic Acid Complexes as Mitochondria-Targeted Imaging and Anticancer Agents, *J. Inorg. Biochem.*, 2022, **233**, 111855.

18 K. Naito, K. Yokoi, C. Balachandran, Y. Hisamatsu and S. Aoki, Design, Synthesis, and Anticancer Activity of Iridium(III) Complex-Peptide Hybrids That Contain Hydrophobic Acyl Groups at the N-Terminus of the Peptide Units, *J. Inorg. Biochem.*, 2019, **199**, 110785.

19 K. Yokoi, C. Balachandran, M. Umezawa, K. Tsuchiya, A. Mitrić and S. Aoki, Amphiphilic Cationic Triscyclometalated Iridium(III) Complex–Peptide Hybrids Induce Paraptosis-like Cell Death of Cancer Cells *via* an Intracellular Ca^{2+}-Dependent Pathway, *ACS Omega*, 2020, **5**(12), 6983–7001.

20 J. Haribabu, Y. Tamura, K. Yokoi, C. Balachandran, M. Umezawa, K. Tsuchiya, Y. Yamada, R. Karvembu and S. Aoki, Synthesis and Anticancer Properties of Bis- and Mono(Cationic Peptide) Hybrids of Cyclometalated Iridium(III) Complexes: Effect of the Number of Peptide Units on Anticancer Activity, *Eur. J. Inorg. Chem.*, 2021, **18**, 1796–1814.

21 E. Guillén, A. González, P. K. Basu, A. Ghosh, M. Font-Bardia, T. Calvet, C. Calvis, R. Messeguer and C. López, The Influence of Ancillary Ligands on the Antitumoral Activity of New Cyclometallated Pt(II) Complexes Derived from an Ferrocene-Pyrazole Hybrid, *J. Organomet. Chem.*, 2017, **828**, 122–132.

22 Y. Yang, L. Guo, X. Ge, Z. Tian, Y. Gong, H. Zheng, Q. Du, X. Zheng and Z. Liu, Novel Lysosome-Targeted Cyclometalated Iridium(III) Anticancer Complexes Containing Imine-N-Heterocyclic Carbene Ligands: Synthesis, Spectroscopic Properties and Biological Activity, *Dyes Pigm.*, 2019, **161**, 119–129.

23 C.-P. Tan, Y.-M. Zhong, L.-N. Ji and Z.-W. Mao, Phosphorescent Metal Complexes as Theranostic Anticancer Agents: Combining Imaging and Therapy in a Single Molecule, *Chem. Sci.*, 2021, **12**(7), 2357–2367.

24 R. Guan, L. Xie, L. Ji and H. Chao, Phosphorescent iridium (III) complexes for anticancer applications, *Eur. J. Inorg. Chem.*, 2020, **42**, 3978–3986.

25 I. A. Schepetkin, M. B. Plotnikov, A. I. Khlebnikov, T. M. Plotnikova and M. T. Quinn, Oximes: Novel therapeutics with anticancer and anti-inflammatory potential, *Biomolecules*, 2021, **11**(6), 777.

26 K. E. Yang, H. J. Jang, I. H. Hwang, Y. H. Chung, J. S. Choi, T. H. Lee, I. S. Jang, *et al.*, Phenyl 2-pyridyl ketoxime induces cellular senescence-like alterations via nitric oxide production in human diploid fibroblasts, *Aging Cell*, 2016, **15**(2), 245–255.

27 N. R. Palepu, S. Adhikari, A. K. Verma, S. L. Shepherd, R. M. Phillips, W. Kaminsky and M. R. Kollipara, Half-sandwich ruthenium, rhodium and iridium complexes featuring oxime ligands: Structural studies and preliminary investigation of in vitro and in vivo anti-tumour activities, *Appl. Organomet. Chem.*, 2017, **31**(7), e3640.

28 M. Alinaghi, K. Karami, A. Shahpiri, A. A. Momtazi-Borojeni, E. Abdollahi and J. Lipkowski, A Pd (II) complex derived from pyridine-2-carbaldehyde oxime ligand: Synthesis, characterization, DNA and BSA interaction studies and in vitro anticancer activity, *J. Mol. Struct.*, 2020, **1219**, 128479.

29 M. M. El-Bendary, T. S. Saleh, M. M. Alomari, E. M. Ali, B. Davaasuren, M. Jaremko and B. A. Babgi, Potential anticancer activities and catalytic oxidation efficiency of Platinum (IV) Complex, *Molecules*, 2022, **27**(14), 4406.

30 K. Charan Pradhan, H. K. Kisan and S. Pal, Unexpected *Ortho* C–H Bond Activation in Coordinated 7,8-Benzoquinoline: Synthesis and Characterisation of Heteroleptic Ir(III)-7,8-Benzoquinoline Complexes, *RSC Adv.*, 2021, **11**(21), 12578–12582.

31 K. C. Pradhan, M. Jadab, S. Barik, N. Behera, B. Bag and S. Pal, Pyridine Aldoxime Ligation to Iridium(III) Centre: An Innocent Ancillary Ligand in a Series of Organometallic Complexes, *J. Mol. Struct.*, 2023, **1271**, 133998.

32 M. Jadab, K. C. Pradhan, S. Behera, S. K. Agrawalla, S. Barik, C. S. Purohit, S. Samanta, M. K. Santra, J. Kumar and S. Pal, Luminescent Platinum (II) Complexes Featuring Innocent Pyridine-2-aldoxime Ligand: Synthesis, Characterization, and Exploration of Their In Vitro Cytotoxicity Properties, *ChemistrySelect*, 2025, **10**(17), e202500328.

33 K. C. Pradhan, M. Jadab, S. Rout, R. Dandela, D. Mandal, T. Parija, S. Barik, J. Kumar and S. Pal, Orange/red light emitting iridium (III) organometallic complexes containing 2, 3-di (pyridine-2-yl) quinoxaline as ancillary ligand and their anticancer properties, *Z. Anorg. Allg. Chem.*, 2023, **649**(22), e202300169.

34 K. Xiong, Y. Chen, C. Ouyang, R. L. Guan, L. N. Ji and H. Chao, Cyclometalated iridium(III) complexes as mitochondria-targeted anticancer agents, *Biochimie*, 2016, **125**, 186–194.

35 A. Zamora, G. Vigueras, V. Rodríguez, M. D. Santana and J. Ruiz, Cyclometalated iridium (III) luminescent complexes in therapy and phototherapy, *Coord. Chem. Rev.*, 2018, **360**, 34–76.

36 R. D. Sanner, N. J. Cherepy, H. Q. Pham and V. G. Young, Phosphorescent Heteroleptic Iridium(III) Cyclometallates: Improved Syntheses of Acetylacetonate Complexes and Quantum Chemical Studies of Their Excited State Properties, *Polyhedron*, 2020, **176**, 114256.

37 Y. You and W. Nam, Photofunctional triplet excited states of cyclometalated Ir (III) complexes: beyond electroluminescence, *Chem. Soc. Rev.*, 2012, **41**(21), 7061–7084.

38 B. S. McGhie and J. R. Aldrich-Wright, Photoactive and luminescent transition metal complexes as anticancer agents: a guiding light in the search for new and improved cancer treatments, *Biomedicines*, 2022, **10**(3), 578.

39 P. Bujak, I. Kulszewicz-Bajer, M. Zagorska, V. Maurel, I. Wielgus and A. Pron, Polymers for electronics and spintronics, *Chem. Soc. Rev.*, 2013, **42**, 8895–8999.

40 F. Du, L. Bai, M. He, W. Y. Zhang, Y. Y. Gu, H. Yin and Y. J. Liu, Design, synthesis and biological evaluation of

iridium (III) complexes as potential antitumor agents, *J. Inorg. Biochem.*, 2019, **201**, 110822.

41 L. Lu, L. J. Liu, W. C. Chao, H. J. Zhong, M. Wang, X. P. Chen and C. H. Leung, Identification of an iridium (III) complex with anti-bacterial and anti-cancer activity, *Sci. Rep.*, 2015, **5**(1), 14544.

42 M. Redza-Dutordoir and D. A. Averill-Bates, Activation of apoptosis signalling pathways by reactive oxygen species, *Biochim. Biophys. Acta Mol. Cell Res.*, 2016, **1863**(12), 2977–2992.

43 B. Xie, Y. Wang, D. Wang, X. Xue and Y. Nie, Synthesis, Characterization and Anticancer Efficacy Studies of Iridium (III) Polypyridyl Complexes against Colon Cancer HCT116 Cells, *Mol. Basel Switz.*, 2022, **27**(17), 5434.

44 W. L. F. Armarego and C. L. L. Chai, *Purification of Laboratory Chemicals*, Elsevier, 6th edn, 2013.

45 M. Nonoyama, Benzo[h]Quinolin-10-Yl-N Iridium(III) Complexes. Bull, *J. Chem. Soc. Jpn.*, 1974, **47**(3), 767–768.

46 F. Neese, The ORCA Program System, *Wiley Interdiscip. Rev.:Comput. Mol. Sci.*, 2012, **2**(1), 73–78.

47 S. Grimme, J. Antony, S. Ehrlich and H. Krieg, A Consistent and Accurate Ab Initio Parametrization of Density Functional Dispersion Correction (DFT-D) for the 94 Elements H-Pu, *J. Chem. Phys.*, 2010, **132**(15), 154104.

48 P. J. Hay and W. R. Wadt, Ab Initio Effective Core Potentials for Molecular Calculations. Potentials for K to Au Including the Outermost Core Orbitals, *J. Chem. Phys.*, 1985, **82**(1), 299–310.

49 W. J. Hehre, R. Ditchfield and J. A. Pople, Self—Consistent Molecular Orbital Methods. XII. Further Extensions of Gaussian—Type Basis Sets for Use in Molecular Orbital Studies of Organic Molecules, *J. Chem. Phys.*, 1972, **56**(5), 2257–2261.

50 P. C. Hariharan and J. A. Pople, The Influence of Polarization Functions on Molecular Orbital Hydrogenation Energies, *Theor. Chim. Acta*, 1973, **28**(3), 213–222.

51 A. V. Marenich, C. J. Cramer and D. G. Truhlar, Universal Solvation Model Based on Solute Electron Density and on a Continuum Model of the Solvent Defined by the Bulk Dielectric Constant and Atomic Surface Tensions, *J. Phys. Chem. B*, 2009, **113**(18), 6378–6396.

52 J. Pradhan, C. Mohanty and S. K. Sahoo, Protective efficacy of crocetin and its nanoformulation against cyclosporine A-mediated toxicity in human embryonic kidney cells, *Life Sci.*, 2019, **216**, 39–48.

53 C. C. Liang, A. Park and J. L. Guan, *In vitro* scratch assay: a convenient and inexpensive method for analysis of cell migration *in vitro*, *Nat. Protoc.*, 2007, **2**, 329–333.

54 N. Franken, H. Rodermond, J. Stap, J. Haveman and C. Bree, Clonogenic assay of cells *in vitro*, *Nat. Protoc.*, 2006, **1**, 2315–2319.

55 E. Bagheri, F. Hajiaghaalipour, S. Nyamathulla and N. A. Salehen, Ethanolic extract of Brucea javanica inhibit proliferation of HCT-116 colon cancer cells *via* caspase activation, *RSC Adv.*, 2018, **8**(2), 681–689.

56 M. N. Breit, W. C. Kisseberth, M. D. Bear, Y. Landesman, T. Kashyap, D. McCauley, M. G. Kauffman, S. Shacham and C. A. London, Biologic activity of the novel orally bioavailable selective inhibitor of nuclear export (SINE) KPT-335 against canine melanoma cell lines, *BMC Vet. Res.*, 2014, **10**(160), 1–11.